J. Fluid Mech. (2009), vol. 620, pp. 63–88. © 2009 Cambridge University Press
doi:10.1017/S0022112008004734 Printed in the United Kingdom

MTV measurements of the vortical field in the wake of an airfoil oscillating at high reduced frequency

DOUGLAS G. BOHL[1]†
AND MANOOCHEHR M. KOOCHESFAHANI[2]

[1]Department of Mechanical and Aeronautical Engineering, Clarkson University, Potsdam, NY 13699 USA

[2]Department of Mechanical Engineering, Michigan State University, East Lansing, MI 48824, USA

(Received 18 July 2008 and in revised form 22 October 2008)

We present an experimental investigation of the flow structure and vorticity field in the wake of a NACA-0012 airfoil pitching sinusoidally at small amplitude and high reduced frequencies. Molecular tagging velocimetry is used to quantify the characteristics of the vortex array (circulation, peak vorticity, core size, spatial arrangement) and its downstream evolution over the first chord length as a function of reduced frequency. The measured mean and fluctuating velocity fields are used to estimate the mean force on the airfoil and explore the connection between flow structure and thrust generation.

Results show that strong concentrated vortices form very rapidly within the first wavelength of oscillation and exhibit interesting dynamics that depend on oscillation frequency. With increasing reduced frequency the transverse alignment of the vortex array changes from an orientation corresponding to velocity deficit (wake profile) to one with velocity excess (reverse Kármán street with jet profile). It is found, however, that the switch in the vortex array orientation does not coincide with the condition for crossover from drag to thrust. The mean force is estimated from a more complete control volume analysis, which takes into account the streamwise velocity fluctuations and the pressure term. Results clearly show that neglecting these terms can lead to a large overestimation of the mean force in strongly fluctuating velocity fields that are characteristic of airfoils executing highly unsteady motions. Our measurements show a decrease in the peak vorticity, as the vortices convect downstream, by an amount that is more than can be attributed to viscous diffusion. It is found that the presence of small levels of axial velocity gradients within the vortex cores, levels that can be difficult to measure experimentally, can lead to a measurable decrease in the peak vorticity even at the centre of the flow facility in a flow that is expected to be primarily two-dimensional.

1. Introduction

Unsteady airfoil flows have received considerable attention in the literature originally due to the need to understand and alleviate the undesirable effects of flutter, buffeting and dynamic stall (Theodorsen 1935; Von Kármán & Sears 1938; McCroskey 1982). These flows have also been the subject of extensive studies with biological applications in connection with the propulsion of flying and aquatic

---

† Email address for correspondence: dbohl@clarkson.edu

animals (Wu 1971; Lighthill 1975). Flapping wing propulsion has been the subject of numerous experimental studies (Oshima & Oshima 1980; DeLaurier & Harris 1982; Freymuth 1988; Koochesfahani 1989; Triantafyllou, Triantafyllou & Grosenbaugh 1993; Anderson *et al.* 1998) with typical chord Reynolds numbers in the range 10^4–10^5 and computational studies, both inviscid (Katz & Weihs 1978; Platzer, Neace, & Pang 1993; Jones & Platzer 1997) and viscous (Stanek & Visbal 1989; Liu & Kawachi 1999; Ramamurti & Sandberg 2001). The connection between the generated wake structure and kinematics of nature's flyers/swimmers is a current subject of active research (Spedding, Hedenström & Rosén 2003; Rosén, Spedding & Hedenström 2004; Dabiri *et al.* 2005). There is also a resurgence of interest in unsteady aerodynamics of flapping wings because of potential applications in micro air vehicle design.

The study of the wake structure of flapping wings is made complicated by the fact that it is influenced by a large number of parameters such as motion type (e.g. heave, pitch, etc.), amplitude, frequency, rigid or flexible surfaces and two-dimensional versus three-dimensional moving surfaces. Even in the simplest case of a two-dimensional airfoil that is harmonically oscillating in pure pitch with low amplitude, the vortical field in the wake is significantly affected not only by the oscillation frequency but also by the shape of the pitch waveform which can result in very intricate vortex patterns (Koochesfahani 1989). Despite the complexities introduced by the various influences, it is well-recognized that the wake of unsteady airfoils is highly vortical and that the essential ingredients of the problem are the generation of vorticity, its shedding and roll up and subsequent evolution/dynamics. For example, thrust development on a flapping airfoil has been explained in terms of the generation of a reversed vortex street and its corresponding jet-like average velocity profile in the wake, as originally described by Von Kármán and Burgers (1943) for a flat plate in transverse oscillation. It is instructive to note that in a large fraction of experimental studies of flapping wings the behaviour of the vorticity field is not directly measured but is inferred from flow visualization (Oshima & Oshima 1980; Freymuth 1988; Koochesfahani 1989) or composite of single-point velocity measurements (Koochesfahani 1989; Wilder *et al.* 1996). More recent studies are applying whole-field velocimetry methods to quantify the properties of the vorticity field in these class of flows (Freymuth 1988; Bohl 2002).

An important issue relevant to studies of flapping wings is the experimental estimation of the mean force (drag/thrust) from wake data. The interest in this approach stems from the difficulty of direct force measurement in flapping wings or actual flying animals, and the additional measurement challenges posed by the very small forces involved in low Reynolds number flight. It is commonplace to estimate the mean force based on the mean streamwise velocity profile using the integral momentum theorem applied to a control volume surrounding the airfoil (Koochesfahani 1989; Anderson *et al.* 1998; Spedding *et al.* 2003). In particular, in the work of Koochesfahani (1989), which is the subject of further scrutiny in the current study, only the mean streamwise velocity profiles were used because data were not available for the velocity fluctuation and pressure terms that would be needed for a complete analysis of momentum integral. Nevertheless, those force estimates have been used in comparative studies with subsequent experiments and computations, resulting in very good agreement (Triantafyllou *et al.* 1993), reasonable agreement (Liu & Kawachi 1999) and very poor agreement (Ramamurti & Sandberg 2001). It is expected that the accuracy of such estimates comes into question with increasing reduced frequency because of both the increased velocity fluctuation level and the reduced pressure in the cores of the concentrated vortices in the wake. A study based on an inviscid Kármán vortex street model of the wake suggests that the use of mean velocity surveys tends to overestimate the thrust force (Streitlien & Triantafyllou 1998). This analysis is qualitative, however, as it does not take into account the viscous characteristics of the vortex street, nor does it account for the pressre reduction in the viscous core. In addition, it is difficult to quantify the inaccuracies in force estimates in actual experiments based on the vortex street model since it requires knowledge of vortex array properties (e.g. circulation, streamwise and lateral spacing, etc.).

The work presented here focuses on quantifying the properties of the vortical field in the wake of a NACA-0012 airfoil pitching harmonically at low amplitude under similar conditions as the previous flow visualization work of Koochesfahani (1989). Because of low amplitude, potential complexities connected to leading-edge flow separation are removed. The emphasis is primarily on the cases with high reduced frequency which may lead to thrust generation for which quantitative data comparable to those presented here do not exist. We utilize Molecular Tagging Velocimetry (MTV) for whole-field measurements of the velocity and vorticity fields over the first chord length downstream of the trailing edge. These data enable the continuous spatial analysis of the development of vortex array and its properties (e.g. circulation, peak vorticity, core size, spatial arrangement, etc.) over the first chord length and allow us to explore the connection between those properties and generation of thrust. We use these data further to quantify the inaccuracy in mean force estimates that are arrived at with the use of only mean streamwise velocity profiles. Such detailed data that are obtained for well-defined experimental conditions should prove useful for validation of computational and modelling efforts. We note that even though the flow is laminar for the Reynolds number considered here, there are spatial and temporal resolution challenges involved in computing such highly unsteady flows; for example, the spatial resolution in the trailing-edge region plays a critical role in capturing the wake vorticity field with high fidelity (Stanek & Visbal 1989).

The paper is organized as follows. Section 2 gives an overview of the experimental set-up, the measurement method and accuracy estimates. Discussion of results is presented in § 3.1 for the detailed behaviour of the vorticity field, followed by the measurements of the velocity field in § 3.2. Finally, the methodology for estimating the mean force is developed in § 3.3 and the results are compared with previous experiments and computations.

2. Experimental set-up

This section gives an overview of the essential elements of experimental arrangement, the measurements technique and data processing. Further details are described in Bohl (2002).

The experiments were conducted in the Turbulent Mixing and Unsteady Aerodynamics Laboratory at Michigan State University in a closed-return water tunnel (Engineering Laboratory Design, ELD) water tunnel with a 61 cm × 61 cm × 243 cm test section. A NACA-0012 airfoil with chord length $C = 12$ cm was placed in a freestream velocity $U_\infty \approx 10.5$ cm s^{-1}, resulting in a chord Reynolds number $Re_c = 12\,600$. This Reynolds number was chosen to closely match the conditions reported in Koochesfahani (1989). The hollow-core airfoil was constructed of a fibreglass laminate using a CNC-machined aluminum mold. The final shape of the constructed airfoil closely matched the NACA-0012 profile, with its thickness varying less than $(8 \times 10^{-4} C)$ from the nominal profile over the entire airfoil (Gendrich 1998). The airfoil was held horizontally in the water tunnel between two

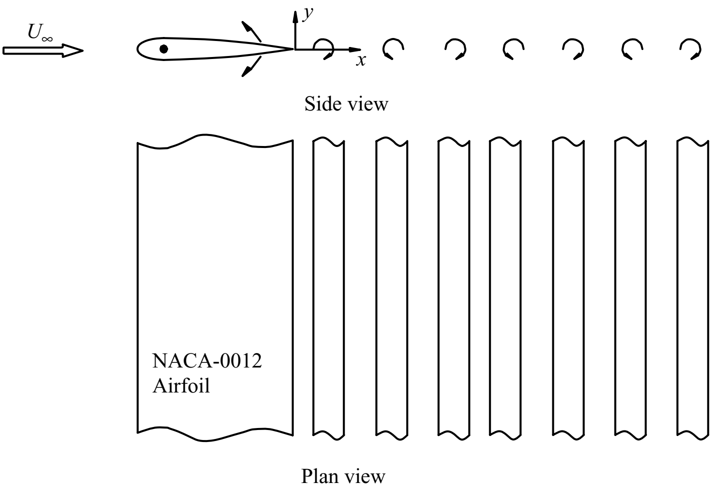

FIGURE 1. Schematic of semi-infinite vortex array in the wake of an airfoil pitching with small amplitude. Note the coordinate system used in this work.

streamlined acrylic false wall assemblies which were hollow and housed the airfoil mounting hardware and drive linkages. The resulting span of the airfoil was 48.5 cm, leading to a geometric aspect ratio of 4. The airfoil oscillated sinusoidally in pitch about its $1/4$-C axis with an amplitude α_o of 2° (i.e. peak to peak amplitude of 4°) about a zero mean angle of attack (AOA) and a frequency f in the range 1.18–3.21 Hz. This corresponds to a reduced frequency $k=(2\pi f\,C)/2U_\infty$ in the range 4.1–11.5. The motion of the airfoil was controlled by a DC servo motor driven by a Galil DMC-1030 digital control system and monitored by a high resolution optical encoder. The deviation of the actual motion of the airfoil from the ideal sine wave was measured to correspond to a peak deviation of 0.07° and an r.m.s deviation over a cycle of 0.02° (Bohl 2002). A schematic of the flow geometry is shown in figure 1.

The measurements presented in this work were made using MTV. Molecular tagging velocimetry is a whole-field optical technique that relies on molecules, uniformly mixed in the fluid medium, which can be turned into long lifetime tracers upon excitation by photons of an appropriate wavelength. Typically a pulsed laser is used to ‘tag’ the regions of interest, and those tagged regions are interrogated at two successive times within the lifetime of the tracer. The measured Lagrangian displacement of the tagged regions provides the estimate of the fluid velocity vector. One might think of the MTV technique as the *molecular* counterpart of particle image velocimetry (PIV) where fluid molecules, rather than seed particles, are marked and tracked. Details of this experimental technique are reviewed elsewhere (Koochesfahani 2000; Koochesfahani & Nocera 2007). The measurements in the current study utilized a grid of intersecting laser lines for tagging purposes, see figure 2, with each intersection providing the two components of the velocity vector projected onto the viewed plane (i.e. u, v).

Water-soluble phosphorescent molecules, with a lifetime of $\tau\approx 3.5$ ms, were the particular long lifetime tracer used in this work. The properties and utilization of this tracer have been previously described (Gendrich, Koochesfahani & Nocera 1997). A pulsed excimer laser (Lambda-Physik, LPX 210i) with 20 ns pulses at a wavelength of 308 nm provided the photon source for the experiments. MTV image pairs (640×480 pixel, 8 bit) were captured using a gated intensified CCD camera (Stanford Computer Optics, SCO 4QuickE) at a rate of 60 images/s, resulting in a velocity data rate of

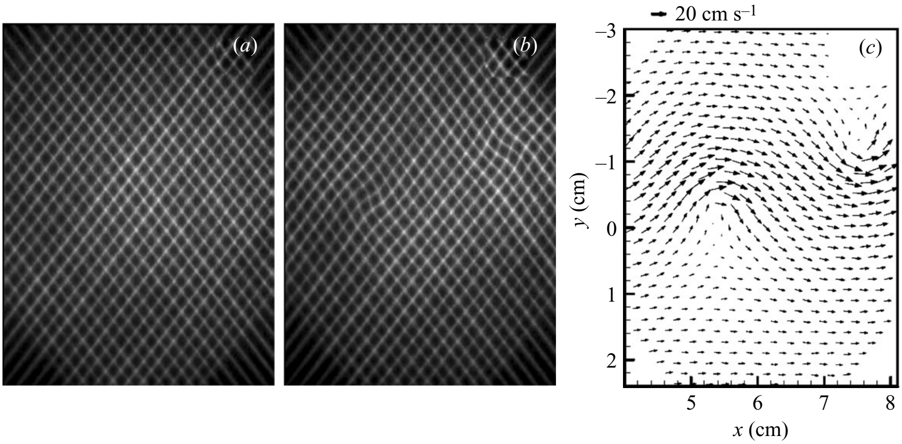

FIGURE 2. Typical MTV image pairs and the resultant two-component velocity vector field in the wake of the oscillating airfoil. (*a*) Undelayed grid imaged 1 μs after the laser pulse ('undelayed' image); (*b*) same grid imaged 3.5 μs later ('delayed' image); and (*c*) velocity field derived from (*a*) and (*b*).

30 Hz. In our previous implementations of MTV, the image pairs were usually acquired by a pair of carefully aligned detectors synchronized using a digital delay generator (Gendrich, Bohl & Koochesfahani 1997; Gendrich, Koochesfahani & Nocera 1997; Gendrich 1998). In the current work, however, the image pairs were acquired with a single intensified camera, where two full-frame images were obtained with a time delay controlled by the intensifier gate pulse sequence. The field of view used in this work was typically 5.5 × 4.2 cm and delay time between image pairs was nominally 3.5 ms and was adjusted to limit the maximum displacement of the tagged regions to about 10 pixels. A direct spatial correlation method (Gendrich & Koochesfahani 1996) was utilized to determine the displacement of the tagged regions.

The flow field under investigation was periodic and could, therefore, be phase averaged quite effectively. In this work, each experimental run consisted of 1000 whole-field measurements that were divided into 64 phases, ϕ, and then averaged. A more detailed explanation of the phase-averaging process can be found in Bohl (2002). The data-processing strategy allowed the data from multiple field of views to be combined into one single data set to create the evolution of the flow field map versus oscillation phase, for each reduced frequency, covering a spatial region from just upstream of the airfoil trailing edge to $x/C = 1.1$ downstream. Phased-averaged quantities are indicated by bracketed $< >$ variables.

The accuracy of instantaneous MTV velocity measurements depends on the signal to noise (S/N) ratio of the image pairs used in the correlation procedure; highly accurate estimates of displacement of tagged regions (i.e. low sub-pixel error) can be achieved with high S/N images (Gendrich & Koochesfahani 1996). An intensified detector, however, is typically noisier than non-intensified CCD detectors. The actual measurement accuracy in this work was quantified experimentally for the particular intensifier voltage level of these measurements, and it was found that the displacement of the tagged regions could be measured with a 95 % confidence level of 0.17 pixel accuracy (Bohl 2002). The corresponding uncertainty level in the velocity measurements was 0.4 cm s^{-1}. Since there were typically 16 independent velocity realizations per phase bin, the error in the reported phase-averaged velocities was reduced by a factor of 4 to 0.1 cm s^{-1} (95 % confidence level).

Spanwise vorticity ω_z was calculated from the measured (u, v) velocity using a fourth order accurate central finite difference scheme (Cohn & Koochesfahani 2000). Uncertainty analysis shows that the uncertainty in spanwise vorticity, $\delta\omega_z$, can be estimated by (Cohn 1999)

$$\delta\omega_z = \frac{1.34}{h}\delta u \tag{1}$$

where δu is the uncertainty in the velocity measurement and h represents the data spatial spacing (see Appendix). The spatial resolution of the data reported here was $h = 0.12$ cm, and the aforementioned phase-averaged velocity uncertainty of $\delta u = 0.1\,\mathrm{cm\,s^{-1}}$ results in an uncertainty level (95 % confidence level) of $1.1\,\mathrm{s^{-1}}$ in the phase-averaged vorticity. This uncertainty level is to be compared with peak vorticity magnitudes in the range 25–160 $\mathrm{s^{-1}}$ for the range of reduced frequencies investigated here.

The vortices in this work are characterized in terms of their peak vorticity magnitude, circulation, core size and streamwise/transverse location in the wake. The accuracy of the measurement of the peak vorticity is dependent on the extent of spatial smoothing caused by the spatial resolution of the measurement (characterized by the data spatial spacing relative to the vortex core size) as well as the method used to calculate the vorticity. Based on a previous study of these effects (Cohn & Koochesfahani 2000) for the results presented here (0.12 cm spatial spacing, 0.4 cm vortex core radius or approximately 3.3 data points per vortex core) the peak vorticity values reported are expected to be accurate to better than 2 % of the actual peak vorticity levels.

3. Results and discussion

The data discussed here were measured at the centre span of the airfoil over a streamwise distance of $-0.1 < x/C < 1.1$. The origin of (x, y) coordinates is at the airfoil trailing edge with the airfoil at the zero AOA (see figure 1). The definition sketch in figure 3 illustrates the nomenclature of vortex array geometric parameters that will be used throughout this paper. The vortex array in this figure is shown in the thrust configuration (i.e. jet-like velocity profile), with vortices of positive (counter-clockwise) circulation (referred to as 'positive' vortices) located at a positive transverse location and vortices of negative (clockwise) circulation (referred to as 'negative' vortices) with negative transverse coordinate. The centre of a vortex is defined by the coordinates (x_c, y_c) of its peak vorticity. The vortex array is characterized by its streamwise spacing, a, and transverse spacing, b. The streamwise spacing is connected to the oscillation frequency f and vortex convection velocity U_c through $af = U_c$. The transverse spacing is defined as $b \equiv y_{c,p} - y_{c,n}$, where $y_{c,p}$ and $y_{c,n}$ indicate the transverse coordinates of positive and negative vortices. According to this definition, the vortex street arrangement with the positive vortex on top, i.e. the jet-like velocity profile, results in $b > 0$, whereas $b < 0$ indicates the arrangement with the negative vortex on top (i.e. the usual wake profile with a velocity deficit). In the discussion of results, we first focus on the behaviour and evolution of the vorticity field, followed by observations about the profiles of the mean and fluctuating velocity, and finally conclude with results on the estimate of force on the oscillating airfoil.

3.1. *Vorticity field*

The phase-averaged vorticity fields $\langle\omega_z\rangle$ for three reduced frequencies of $k = 5.2$, 5.7 and 11.5 are shown in figure 4. These specific cases were selected for discussion

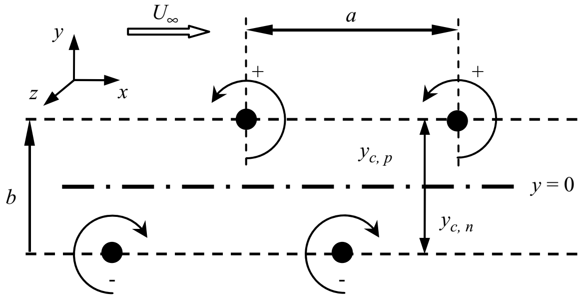

FIGURE 3. Definition of vortex array spacing parameters. Centre of vortex is defined by the spatial location of peak vorticity.

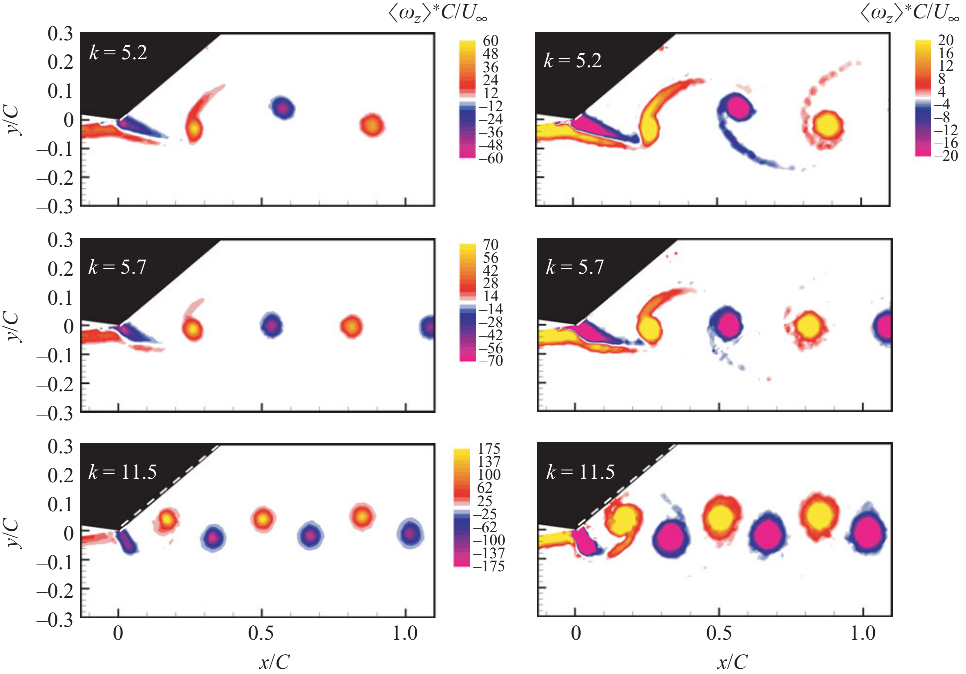

FIGURE 4. Phase-averaged vorticity field in the wake of the oscillating airfoil for three reduced frequencies, $\alpha_o = 2°$. Airfoil is shown at an AOA of 0° with the airfoil pitching down (trailing edge moving up). Dashed lines indicate the boundary of the region where laser beams were blocked by airfoil. Note that the colour assignment to contour levels for the left column is different in the three cases and the contour levels are adjusted to highlight the peak vorticity. The right column shows the same data with contour levels adjusted to highlight the lower vorticity values in the regions at the expense of saturating the high vorticity levels.

because they highlight the essential features of the wake structure at the high reduced frequencies studied in this work. The phase shown in figure 4, $\phi = 0$, corresponds to the airfoil at an AOA of 0°, as it is pitching down (i.e. trailing edge moving up). The black region above the airfoil marked by a dashed line does not contain any data due to blockage of laser beam by the airfoil.

For all three cases shown in figure 4 the boundary layer vorticity originating from the two sides of the oscillating airfoil quickly rolled up into an array of compact isolated vortices of alternating sign. The distinction between the three cases is in the transverse arrangement of the vortex street. For the 'low' reduced frequency, $k = 5.2$, the vortices with negative (clockwise) sign vorticity were located at a y-location greater than the vortices with positive (counter clockwise) sign vorticity. In this case, $y_{c,p} < y_{c,n}$, resulting in $b < 0$, and the transverse orientation of the vortices in the wake was the same as the vorticity in the airfoil boundary layer (i.e. negative vorticity in the top surface boundary layer and positive in the bottom). As the reduced frequency increased to $k = 5.7$, the alternating sign vortices became nearly aligned along a straight line (i.e. $y_{c,p} \approx y_{c,n}, b \approx 0$). For the high reduced frequency, $k = 11.5$, the transverse orientation of the vortices switched compared to the low frequency case so that the positive vortices were now at a y-location greater than the negative vortices (i.e. $y_{c,p} > y_{c,n}$, therefore, $b > 0$). The progression just described, the rearrangement of the transverse positions of the vortices in the vortex street with increasing frequency, is consistent with the previous results arrived at by flow visualization (Koochesfahani 1989).

Several other observations about the initial formation of the vortices in figure 4 are noteworthy. The vorticity layer shedding from the airfoil trailing edge was noted to be connected to the first rolled-up vortex for the lower frequency $k = 5.2$, along with a thin vorticity layer (i.e. braid) that connected the first three alternating vortices for this case (see the right column in figure 4 with contour levels adjusted to highlight the braid regions; the large dynamic range of the vorticity field does not allow the weak vorticity levels in the braids to be highlighted with the colour lookup table of the left column). The thickness of the braids and the vorticity level in them decreased with downstream distance (for a given k) to below detection limits of the measurements. A similar decrease was observed with increasing frequency, k, for a fixed downstream location. The high reduced frequency case, $k = 11.5$, showed no evidence of the connecting vorticity beyond the first pair of vortices. That the regions between vortices are devoid of vorticity has also been noted by Wilder *et al.* (1996). On the contrary, well-resolved braid regions could be seen over the first chord length in the case of the lowest frequency $k = 4.1$ in our experiments (Bohl 2002) (data not shown here). These results indicate that the downstream formation length $X_{formation}$ of the vortices decreased with increasing reduced frequency. It was generally observed that the isolated vortices were formed within the first wavelength, i.e. $X_{formation} \leqslant a$. Using the approximation for the vortex convection speed $U_c \approx U_\infty$ (data in figure 9 show maximum U_c is about 25 % faster than free stream speed), one can show that the formation length is given as a fraction of chord length by $X_{formation}/C \leqslant \pi/k$. For the three reduced frequencies $k = 5.2$, 5.7 and 11.5 illustrated in figure 4, the resulting vortex formation distance is $X_{formation}/C \leqslant 0.60$, 0.55 and 0.27. We note that the formation length is remarkably short for high frequencies, e.g. for $k = 11.5$ the first vortex is formed within the first $1/4\ C$.

In order to determine the actual vorticity distribution within a fully formed vortex, the horizontal profiles of the vorticity field (i.e. vorticity variation with x) through the centre of a vortex located at $x/C = 0.5$ was extracted from the vorticity maps of figure 4. Results are shown in figure 5 for the two cases of $k = 5.2$, and 11.5. Also shown for completion are the profiles of azimuthal velocity V_θ (same as v component of velocity in this case). According to figure 5, the measured vorticity profiles agreed very closely with a Gaussian distribution of vorticity $\omega(r) = \omega_{peak} \exp(-r^2/r_c^2)$ over the core region ($r_c \approx 0.4$ cm) with only small deviations at the outer edge of the distribution (e.g. the right edge of the profile for $k = 11.5$). As expected, the agreement was equally good when comparing the measured profiles of azimuthal velocity against

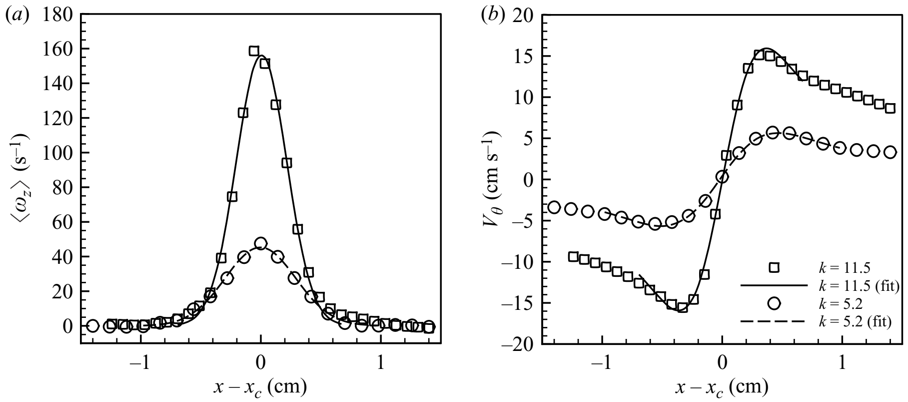

FIGURE 5. Horizontal profiles of (*a*) spanwise vorticity and (*b*) azimuthal velocity taken from a vortex at $x/C = 0.5$ for $k = 5.2$ and 11.5. The distance $(x - x_c)$ is the horizontal distance measured from the centre of the vortex. Solid and dashed curves indicate curve fits to vorticity and azimuthal velocity profiles for a Gaussian distribution of vorticity, $\omega = \omega_{peak}\, \mathrm{e}^{-((x-x_c)^2/r_c^2)}$.

those caused by a Gaussian vorticity field. The increasing deviation as one moves away from the core region, particularly noticeable for the case $k = 11.5$, reflects primarily the contributions from the induced velocity of neighbouring vortices. We note that the maximum azimuthal (swirl) velocity increases with reduced frequency and can become a sizeable fraction of freestream speed. For example, for $k = 11.5$ the magnitude of the peak azimuthal velocity is about 1.5 U_∞, i.e. the instantaneous streamwise velocity reverses direction towards upstream with a magnitude as high as 0.5 U_∞.

The vortex array pattern and its change with increasing frequency (see figure 4) lead to interesting consequences for the mean and fluctuating vorticity, ω_{avg} and $\omega_{r.m.s}$, as illustrated in figure 6. In this figure the mean and r.m.s vorticity fields of the stationary airfoil (airfoil fixed at zero AOA) are also included for reference and we will discuss them first because they did exhibit certain unique features. In the case of stationary airfoil, the opposite sign vorticity from the two sides of the airfoil smoothly left the trailing edge into the wake region while reducing in magnitude with downstream distance. The very near-wake was characterized by a steady region of recirculation that extended to $x/C \approx 0.1$ and a wake whose thickness actually decreased until about $x/C \approx 0.5$ (see § 3.2 and Bohl 2002). It was beyond this location that a typical wake behaviour was observed, with a width increasing with downstream distance along with a rapidly decreasing peak vorticity. The vorticity fluctuation for the stationary airfoil was relatively weak and its maximum value occurred in the region around $x/C = 0.5$.

For the case of $k = 5.2$ there were thin regions immediately after the trailing edge where the mean vorticity was of opposite sign to the corresponding boundary layer vorticity on that side. These regions corresponded to the initial formation process of the vortices which were still connected to the boundary layer vorticity (see earlier discussion). The transverse spreading of these regions and their decrease in magnitude farther downstream were the signature of the connecting braids. Once the isolated vortices were formed, two well-defined peaks of opposite vorticity were noted in the mean vorticity with their transverse location and sign of vorticity consistent with the pattern of isolated vortices seen earlier in figure 4 (i.e. $b < 0$ for this case). We also

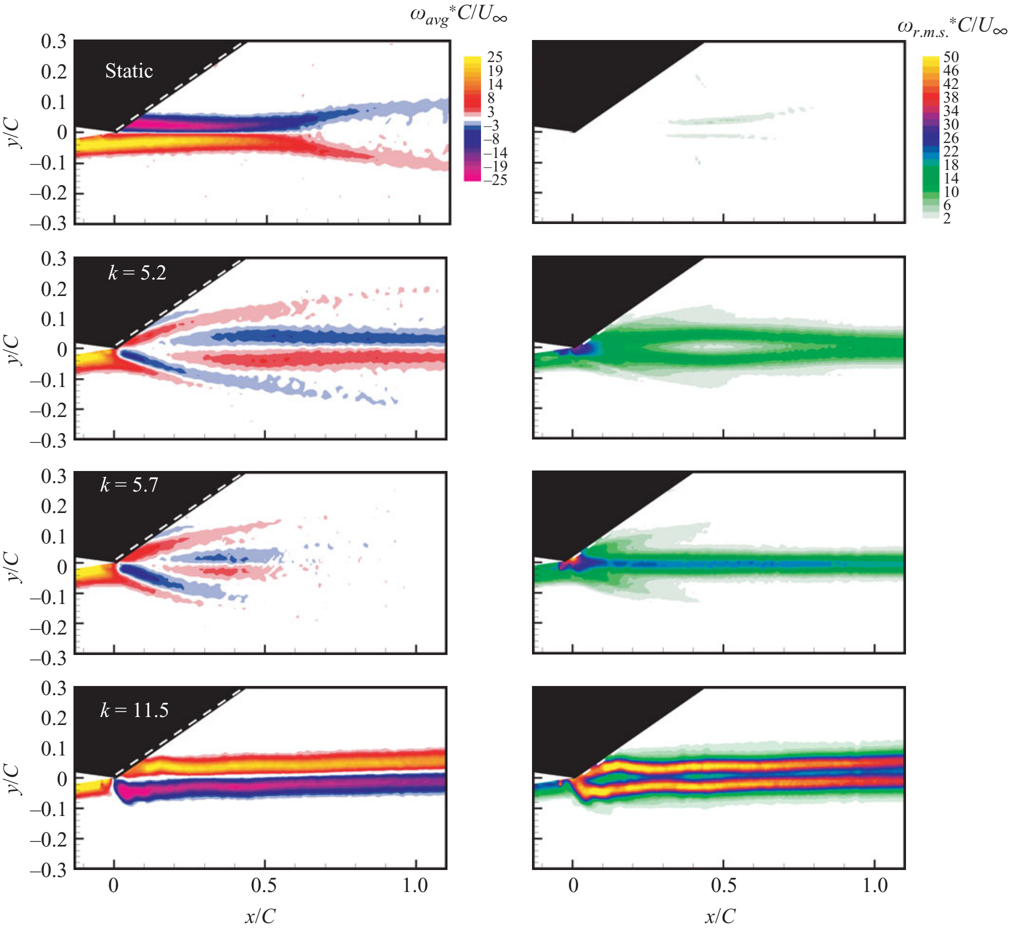

FIGURE 6. Mean and r.m.s vorticity fields, ω_{avg} and $\omega_{r.m.s}$, in the wake of static and oscillating airfoil for the conditions in figure 3.

note that the spacing between the peaks initially increased, followed by a decrease to an asymptotic value by $x/C \approx 1$. The vorticity fluctuation in this case increased significantly compared to the stationary airfoil as one would expect from a convecting array of concentrated vortices. The locations of the two r.m.s vorticity peaks and their downstream evolution are the signature of the particular vortex array in this case (see earlier comments).

These general observations about the structure of the mean vorticity in the initial formation region at the trailing edge also applied to the case of $k = 5.7$. The remarkable feature of this case, however, was the fact that beyond about $x/C \cong 0.5$ the mean vorticity was nearly zero throughout. The implication of this result is that the alternating vortices had to be perfectly lined up along a straight line and the vorticity distribution of vortices had to be nearly identical except for a change of sign. A consequence of this vortex array arrangement was the high level of vorticity fluctuation with a single peak that was confined to a thin region corresponding to the transverse extent of concentrated vortex cores. As the oscillation frequency increased to $k = 11.5$, the mean vorticity developed two well-defined peaks of opposite vorticity right at the trailing edge, indicating the rapid formation of the vortex array, as already discussed in figure 4. The sign of the mean vorticity peaks, however, was opposite of the case with $k = 5.2$, consistent with the transverse arrangement of the vortices shown in figure 4 with $b > 0$. Note that the spacing between the mean vorticity peaks showed a wavy pattern initially before it approached a fixed spacing farther downstream. The vorticity fluctuation, in this case, was extremely high with a peak value that was typically twice the peak of the mean vorticity. The spatial structure of the vorticity r.m.s reflected the same initial wavy pattern noted in the mean vorticity and two strong peaks connected to the passage, an alternating vortex array that is separated laterally.

An important aspect of the mean vorticity fields depicted in figure 6 is the large spatial gradients in vorticity near the airfoil trailing edge for high reduced frequencies. We note that in all four cases (one stationary and three oscillating cases) the mean vorticity field is anti-symmetric about the x-axis (i.e. $\omega_{avg}(y) = -\omega_{avg}(-y)$), as expected. The case of the highest reduced frequency ($k = 11.5$) had only a slight tilt (about 1°) upwards. The downstream variation of the spacing between the peaks of the mean and r.m.s vorticity discussed above for the three oscillating cases is connected to the downstream evolution of the individual vortices in the wake. This aspect will be discussed later more quantitatively when we present the evolution of vortex spacing b by tracking the motion of individual vortices.

The phase-averaged vorticity data such as those in figure 4 allow us to interrogate the downstream evolution of vortex properties, which we present here for the three representative reduced frequencies under discussion. The properties we consider here are the circulation Γ, core size r_c, peak vorticity $\langle\omega_z\rangle_{peak}$ and vortex array transverse spacing b. The first three properties were calculated for vortices of both sign but, because the properties matched very closely, the results are given here only for the positive vortex. The vortex circulation was computed from the area integral of the measured phased-averaged vorticity using two criteria. Only vorticity magnitudes over a cut-off limit of $2\,\mathrm{s}^{-1}$ were included in order to exclude the measurements below the vorticity measurement noise floor (see § 2). In addition, the integration area was limited to a maximum radius of 1 cm from vortex centre (i.e. location of its peak vorticity) to minimize the contributions from the neighbouring vortices of opposite sign and the connecting braids; see figure 6 for justification of this selection. The combination of these two criteria led to a conservative estimate of $2\,\mathrm{cm}^2\,\mathrm{s}^{-1}$ for the uncertainty in the calculation of circulation (Bohl 2002). Using the same two criteria in the calculation of circulation, the vortex core size was characterized in terms of the radius of gyration of the vorticity field, defined by

$$r_c = \sqrt{\frac{\int\!\!\int r^2 \langle\omega_z\rangle \,\mathrm{d}A}{\int\!\!\int \langle\omega_z\rangle \,\mathrm{d}A}}. \tag{2}$$

The radius of gyration is one way to define an effective size for a vortical region when the vorticity field deviates from the Gaussian distribution, is not symmetric or is not yet fully formed. It can be shown that for a vortex with a Gaussian vorticity distribution the radius of gyration is the same as the vortex core radius traditionally defined by the $1/e$ point of the Gaussian-distributed vorticity (Cohn 1999). Generally, the deviation of the vorticity from the Gaussian distribution, especially in the outer edges of the vortex (see figure 5), leads to a radius of gyration that is larger than the

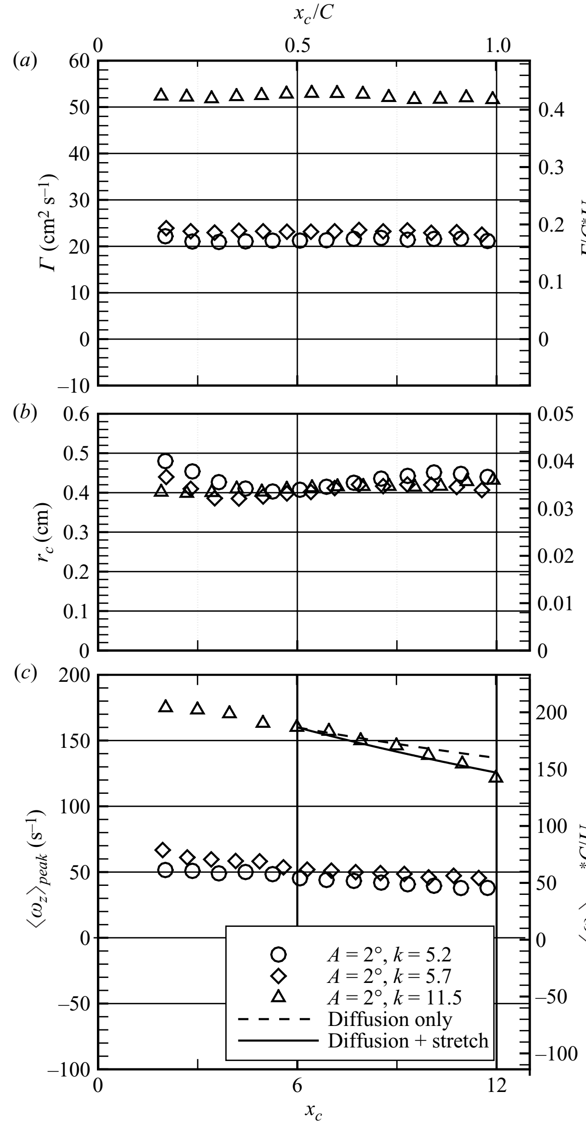

FIGURE 7. Vortex parameters: circulation Γ, vortex core radius r_c and peak vorticity $\langle\omega_z\rangle_{peak}$ as a function of vortex core downstream location x_c for $k = 5.2$, 5.7 and 11.5; $\alpha_o = 2°$. Estimates of the effects of viscous diffusion only and combined viscous diffusion and stretching (0.17 s^{-1}) on the reduction of peak vorticity are shown with dashed and solid lines, respectively.

core radius estimated from the $1/e$ point for the portion of the data in the central region of the vortex. For the data presented here, this difference is typically about 15 %–20 %.

The downstream evolution of phase-averaged vortex circulation Γ, core size r_c, and peak vorticity $\langle\omega_z\rangle_{peak}$ is illustrated in figure 7 (a–c) for the three representative frequencies. For each frequency, the vortex circulation remained constant over the downstream distance investigated, indicating that the vorticity of a vortex remained within the contour selected for the calculation of circulation and also the vorticity of opposite sign did not enter this contour. The increase of circulation with oscillation frequency that is noted in this figure will be discussed further when the data for all the reduced frequencies in this study will be presented (see figure 9).

The vortex core size, r_c, showed a noticeable decrease initially for the two cases of $k = 5.2$ and 5.7, whereas the case of $k = 11.5$ did not exhibit this behaviour. This trend is connected to the vortex formation process discussed earlier, i.e. the evolution of the distributed vorticity field shed from the trailing edge into compact isolated regions of vorticity took place over a greater downstream distance for the lower range of reduced frequencies, and for the highest reduced frequency vortex formation was complete very close to the trailing edge. It is interesting to note that once the vortices were formed by $x/C \approx 0.5$, the core size was the same ($r_c \approx 0.4\,\mathrm{cm}$) for the three reduced frequencies shown in figure 7(*b*). After the initial formation process, the radius of the vortices slowly expanded primarily due to viscous diffusion. This aspect is further discussed next as we isolate the processes that cause the measured variations in the peak vorticity.

The downstream variation of peak vorticity, depicted in figure 7(*c*), showed a continuously decreasing trend for all three cases. We provide an explanation for this behaviour using the vorticity transport equation and for this purpose we will focus on the case of the highest reduced frequency $k = 11.5$. Assuming a primarily two-dimensional flow field, with $\omega_z(r)$ as the predominant component of vorticity and negligible radial component of velocity, the vorticity transport equation reduces to

$$\frac{\partial \omega_z}{\partial t} = \underbrace{\omega_z \frac{\partial w}{\partial z}}_{\mathrm{I}} + \underbrace{\nu \left(\frac{\partial^2 \omega_z}{\partial r^2} + \frac{1}{r} \frac{\partial \omega_z}{\partial r} \right)}_{\mathrm{II}}. \tag{3}$$

Therefore, vorticity can change through two mechanisms: vortex stretching (term I) and viscous diffusion (term II). Vortex stretching is connected with the spanwise gradient of axial velocity in the vortex core, $\partial w/\partial z$. It is known that in the flow studied here, interaction of concentrated vortices with the side walls of the flow facility leads to a spanwise or ‘axial’ flow in the vortex cores along the axis of the vortex (e.g. Koochesfahani 1989; Cohn & Koochesfahani 1993; Bohl & Koochesfahani 2004). The axial flow is away from the side walls towards the centre span and, since by symmetry the axial velocity is zero at centre span, we expect $\partial w/\partial z < 0$ at the centre plane measurements in our study. Therefore, any non-zero value of this velocity gradient would result in a reduction of peak vorticity downstream. The viscous diffusion term, of course, leads to a reduction of peak vorticity as well.

The evolution of vortex peak vorticity can now be determined by evaluating (3) at the centre of the vortex ($r = 0$). On the basis of the earlier discussion showing the vorticity distribution in the rolled-up vortices as well approximated by a Gaussian distribution, it can be shown that the evolution equation for the peak vorticity becomes

$$\frac{\partial (\omega_z)_{peak}}{\partial t} = \underbrace{(\omega_z)_{peak} \frac{\partial w}{\partial z}}_{\mathrm{I}} - \underbrace{\frac{4\pi \nu}{\Gamma} (\omega_z)^2_{peak}}_{\mathrm{II}}. \tag{4}$$

In the equation above, ν is the kinematic viscosity of the fluid (in this case, water), Γ is the vortex circulation given by $\Gamma = \pi r_c^2 (\omega_z)_{peak}$ and it is understood that the axial velocity gradient $\partial w/\partial z$ is that at the centre of the vortex. The evolution of peak vorticity imposed by term I alone corresponds to an exponentially decreasing vorticity (for a constant $\partial w/\partial z < 0$), whereas the solution based on term II alone is the known viscous decay of vorticity with a $1/t$ dependence. The general solution of (4) for a constant value of $\partial w/\partial z$ can be shown to be given by

$$\frac{(\omega_z)_{peak}}{\omega_o} = \frac{\beta}{(\alpha\,\omega_o + \beta)\,\mathrm{e}^{-\beta(t-t_o)} - \alpha\,\omega_o}, \tag{5}$$

where $\beta \equiv \partial w/\partial z, \alpha \equiv -4\pi\nu/\Gamma$ and ω_o is the initial condition of peak vorticity at t_o. The downstream variation of peak vorticity can now be determined from the above using the vortex convection speed, i.e. $(x - x_o) = U_c(t - t_o)$.

We compare the results for the case $k = 11.5$ against the prediction of (5) by specifying the initial conditions at $x_o = 6$ cm (i.e. $x_o/C = 0.5$) where $\omega_o = 160$ s^{-1} (see figure 7*c*). For this reduced frequency, the measurements indicate a vortex circulation $\Gamma = 53.5$ cm^2 s^{-1} and a convection speed $U_c = 13.1$ cm s^{-1} (see figure 9). Over the downstream range considered here ($x - x_o = 6\surd$ cm) and small values of axial velocity gradient (an assumption that will be justified shortly), we note that $\beta(t - t_o) \ll 1$ and $\alpha\,\omega_o(t - t_o) \ll 1$ and (5) can be well represented by its leading-term expansion in $(t - t_o)$, i.e.

$$\begin{aligned}\frac{(\omega_z)_{peak}}{\omega_o} &= 1 + (\alpha\,\omega_o + \beta)(t - t_o) + \cdots \\ &= 1 + (\alpha\,\omega_o + \beta)(x - x_o)/U_c + \cdots\end{aligned} \tag{6}$$

Therefore, to first order, the peak vorticity decreases linearly in downstream distance at a rate determined by the superposition of the effects of viscous decay and vortex stretching. The prediction for the variation of peak vorticity caused by viscous decay only (i.e. $\beta \equiv \partial w/\partial z = 0$), shown in figure 7(*c*) by the dashed curve, indicates that about 70 % of the measured 21 % drop in peak vorticity at the end of the observation domain ($x = 12$ cm; $x/C = 1$) is accounted for by viscous diffusion. The remaining 30 % of the overall peak vorticity drop can be accounted for by the vortex stretching term with an axial velocity gradient of about $\partial w/\partial z \approx -0.17$ s^{-1}. The decrease of peak vorticity predicted from the combination of these two effects is shown by the solid curve in figure 8(*c*). We note that the estimate of $\partial w/\partial z$ that is arrived at here is very small compared to the velocity gradients represented by the measured peak vorticity level of 160 s^{-1} and certainly well below our detection limit for velocity gradients discussed in § 2. It is important to recognize that very small values of $\partial w/\partial z$, which may be difficult to measure experimentally, can still lead to a measurable decrease in the vortex peak vorticity in a flow that is 'expected' to be primarily two-dimensional. In the measurements reported here, the vortex aspect ratio, defined by the ratio of its length to core diameter, was about 60. Nevertheless, the three-dimensional effects of the axial flow caused by the bounding tunnel walls could be detected in the behaviour of peak vorticity even at the centre of the tunnel.

We had earlier connected the spatial structure of the spacing between the peaks of the mean and r.m.s vorticity to the downstream evolution of the individual vortices in the wake. We now discuss this aspect quantitatively by presenting the downstream evolution of vortex spacing b as determined from tracking the trajectories of individual vortices. Figure 8 illustrates the measured variation of the transverse coordinates of positive and negative vortices, $y_{c,p}$ and $y_{c,n}$, along with the vortex array transverse spacing $b \equiv y_{c,p} - y_{c,n}$. Results for $k = 5.2$ show that during the formation process the vortex array initially moved apart over the first half chord downstream to a maximum separation of about $b = -0.89$ cm ($b/r_c \approx 2.2$) before moving back towards each other and approaching a constant vertical spacing at about $x/C \approx 1$ with the negative vortex on top. The vortex array in the $k = 5.7$ case moved towards each other initially

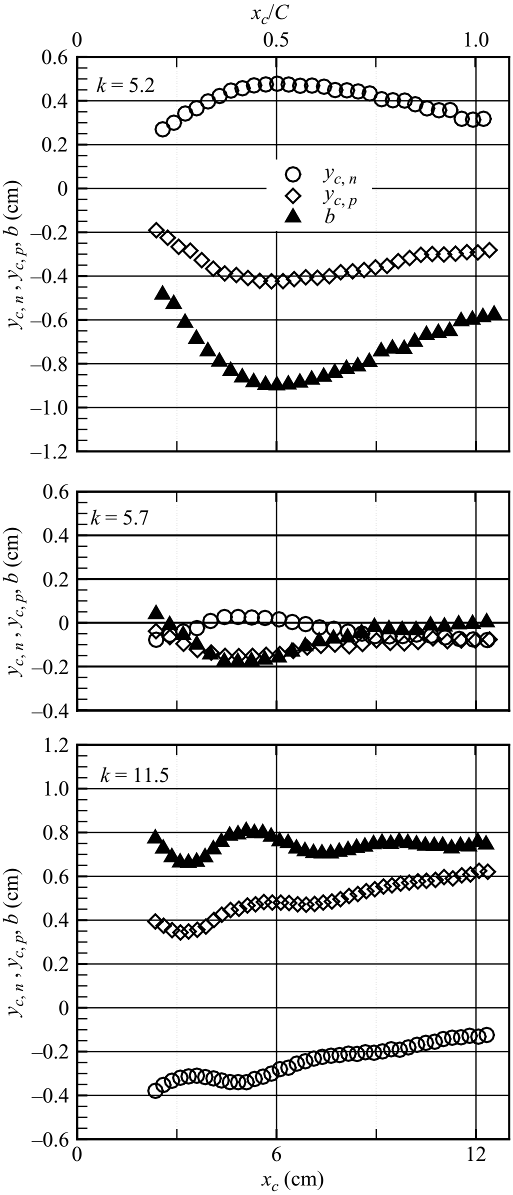

FIGURE 8. Transverse locations of the positive, $y_{c,p}$, and negative vortex, $y_{c,n}$, and the corresponding transverse spacing, b, of vortex array for $k = 5.2$, 5.7, 11.5.

and showed an orientation switch at $x/C \approx 0.25$. This was followed by a period of slight separation, with a maximum of about $b = –0.18$ cm ($b/r_c \approx 0.45$), and then recovery to a constant transverse spacing of $b \approx 0$ corresponding to an alternating vortex array nearly perfectly aligned along a straight line. The high frequency case of $k = 11.5$ was unique in that the transverse vortex array spacing initially had a weak, but discernable, oscillatory behaviour with a maximum amplitude of only about 0.4 r_c. The oscillation quickly damped out and the vortex array attained a transverse

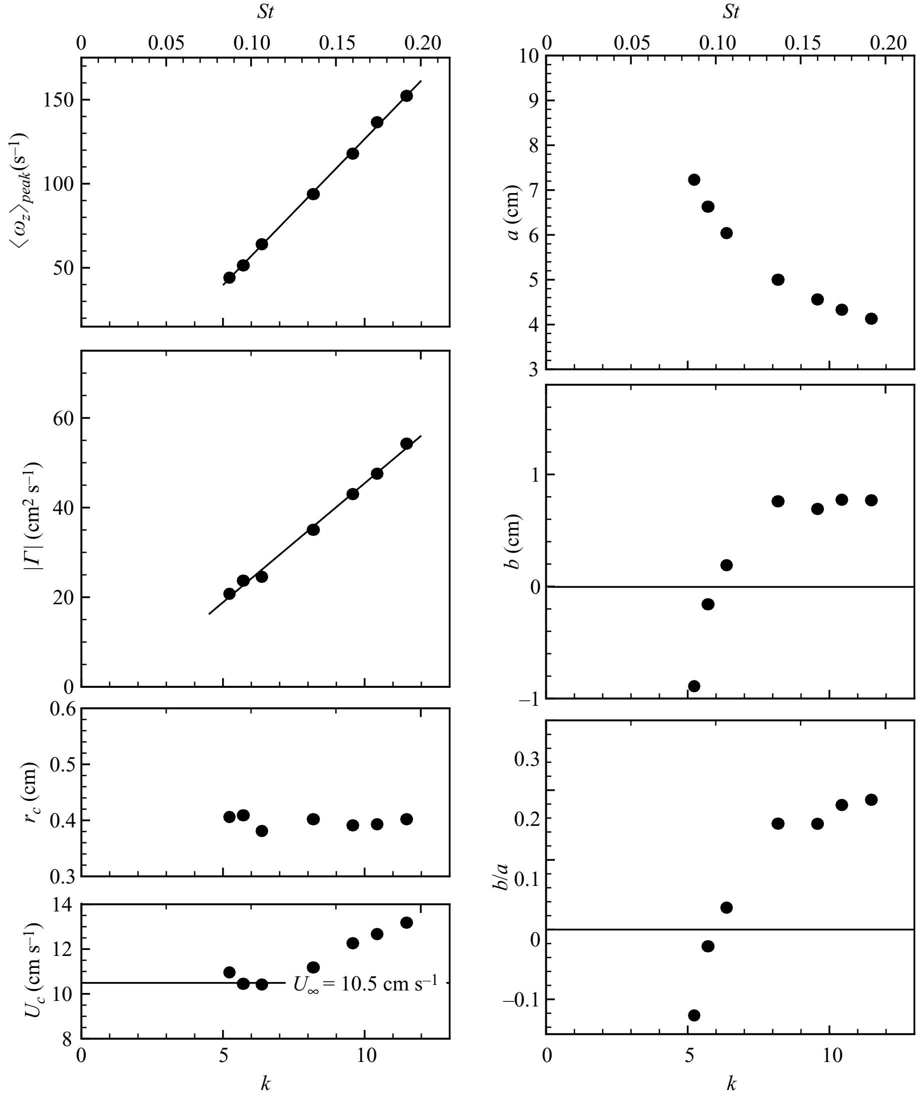

FIGURE 9. Selected vortex properties as a function of reduced frequency at $x/C = 0.5$ downstream of the airfoil-trailing edge. An alternate form of non-dimensional frequency is also indicated in terms of Strouhal number defined by $\mathrm{St} \equiv fA/U_\infty$, where A denotes the peak-to-peak displacement of the airfoil-trailing edge (Triantafyllou *et al.* 1993).

spacing with the positive vortex on top (i.e. $b > 0$). The downstream evolution of the transverse spacing of the concentrated vortex array that was just described for the three selected frequencies explains the unique spatial structure of the vorticity mean and r.m.s discussed earlier in figure 6.

Results presented so far have focused on the detailed behaviour for three repetitive reduced frequency cases. We now show data in figure 7 for several properties of the vortex array at a fixed downstream location and how they vary over the entire range of oscillation frequencies investigated here. The location $x/C = 0.5$ was selected for presenting the results since the vortex array was fully formed by this location (e.g. see figure 4). Data in figure 9 show a linear relationship between the peak vorticity and circulation with increasing reduced frequency. There was a nominal three times increase in the peak vorticity observed over the reduced frequency range indicated in figure 9. It is interesting that the vortex core radius was nearly constant with a value $r_c \approx 0.4\,\mathrm{cm}$ over the entire reduced frequency range. The vortex convection speed was initially very close to the free stream speed U_∞ but started to exceed it by a noticeable amount as the oscillation frequency kept increasing. For the highest reduced frequency of $k = 11.5$ the vortex convection speed was 25 % faster the free stream speed. The vortex array streamwise spacing (wavelength) a is related to the oscillation frequency f and vortex convection velocity U_c according to $af = U_c$. Therefore, the decrease of vortex array wavelength with increasing frequency, indicated in figure 9, was slower than being proportional to $\sim 1/\mathrm{f}$ because of the increase in the vortex convection speed. The vortex transverse spacing b was initially negative, corresponding to the negative vortices forming the top row. With increasing frequency, the spacing decreased towards zero (i.e. alternating vortex array aligned along a straight line) and then switched to a positive sign with the positive vortices being on top. The intriguing result is that the vortex spacing seemed to approach a constant value ($b \approx 0.75\,\mathrm{cm}$) at high reduced frequencies. The vortex array aspect ratio, b/a, showed a trend similar to transverse spacing b except that at large values of reduced frequency the aspect ratio continued to exhibit a slight increasing trend due to the reduction of wavelength a. The largest value of aspect ratio was about 0.19 at the highest frequency shown in figure 9. We note, for comparison, that the vortex array aspect ratios measured in these experiments are noticeably lower than the Kármán value of 0.28 for a stable point vortex street.

3.2. *Velocity field*

The alterations in streamwise velocity field caused by changes in the vortex array pattern with increasing frequency are illustrated in figure 10 in terms of the spatial maps of the mean and r.m.s velocity fields u_{avg} and $u_{r.m.s.}$. The characteristics of the stationary airfoil are also included for comparison. The downstream variation of the mean streamwise velocity at the centreline ($y = 0$) is extracted from the data in figure 10 and separately shown in figure 11 to help with the interpretation of results.

The stationary airfoil was characterized by a near-wake with a region of recirculation that extended to $x/C \approx 0.1$. This aspect is more clearly seen in figure 11, where a very weak reverse flow (i.e. upstream flow) is indicated in this region with a magnitude of about 0.04 U_∞. The recirculation zone was nearly steady as seen by the very low r.m.s values in figure 10. It is also seen that the wake thickness initially decreased until about $x/C \approx 0.5$ and it was beyond this point that the wake width started to increase (see the width of the mean and r.m.s distributions in figure 10). This point also marked the approximate location where the r.m.s fluctuation reached its maximum value. The wake deficit at the centreline continuously decreased with downstream distance and by $x/C = 1$ the average streamwise velocity had reached a value $u_{avg} \approx 0.85\ U_\infty$.

The mean velocity fields for the three representative oscillation frequencies shown in figure 10 confirm that as the reduced frequency increased from $k = 5.2$ to $k = 11.5$ the mean flow's character changed from a wake with a velocity deficit to a jet with a velocity excess. The case $k = 5.7$ showed a mean velocity map that deviated very little from the free stream speed U_∞ except in a small region right at the trailing edge. Examining the mean centreline speed in figure 11 reveals that in all three cases the mean streamwise velocity at the trailing edge was positive and significant ($u_{avg} > 0.5\ U_\infty$) compared to the static case, and it initially increased very quickly.

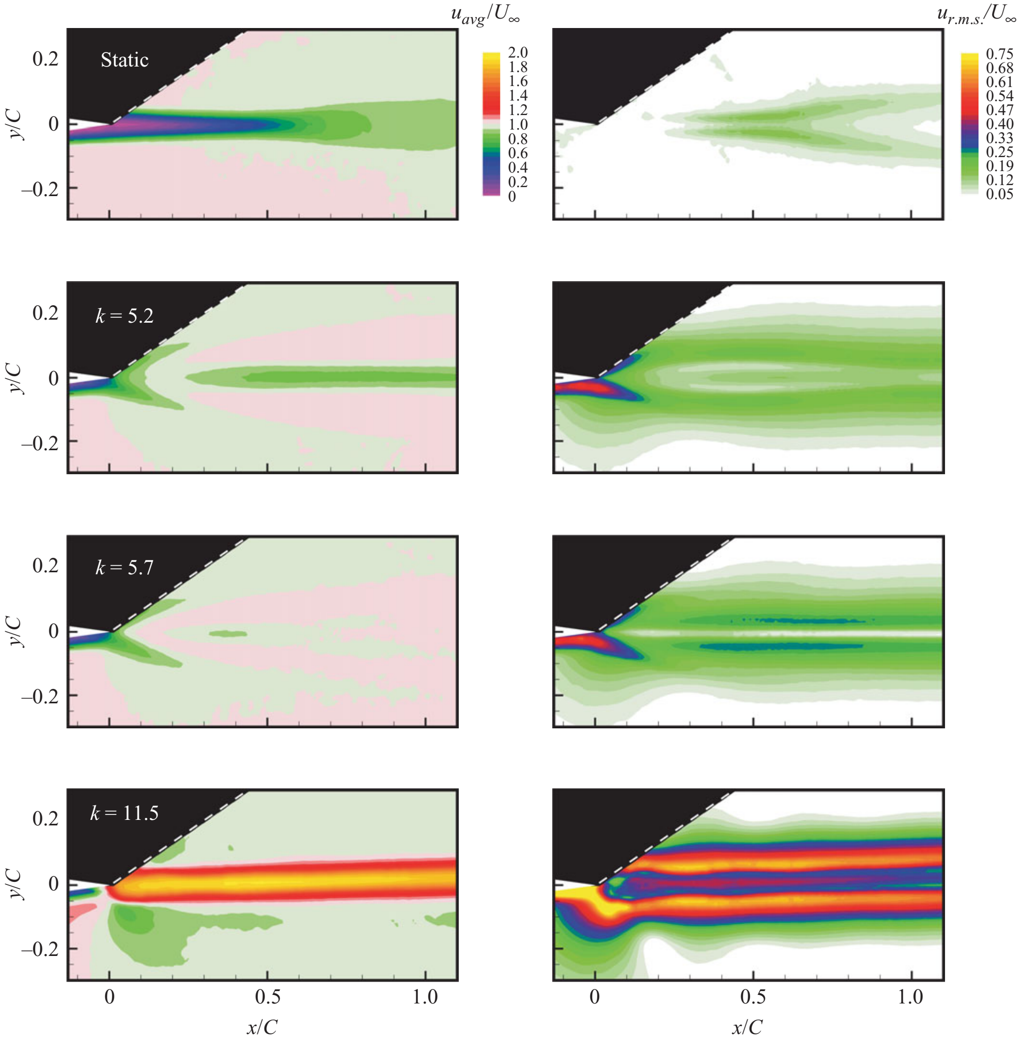

FIGURE 10. Mean and r.m.s streamwise velocity fields, u_{avg} and $u_{r.m.s}$, in the wake of static and oscillating airfoil for the conditions in figure 3.

We caution, however, that the actual mean velocity at the trailing edge ($x \equiv 0$) is not highly resolved due to the finite spatial resolution of the measurements. In the case with a wake-like character ($k = 5.2$), the mean centreline speed remained nearly fixed at $u_{avg} \approx 0.85\ U_\infty$ beyond $x/C \approx 0.4$, whereas the higher frequency jet-like case ($k = 11.5$) had a large velocity excess, reaching values as high as $u_{avg} = 1.94\ U_\infty$. In the case of $k = 5.7$, beyond the initial development zone, the centreline speed has a zero deficit (i.e. $u_{avg} = U_\infty$) except for a small 'dip' centred around $x/C \approx 0.35$. All of these velocity characteristics are consistent with the vortex array structure that has been previously described for each case. The small centreline velocity dip that was just mentioned for $k = 5.7$, for example, can be explained by the slight separation of the vortex array (maximum $b = –0.18$ cm, as discussed earlier) causing a small wake deficit. The spatial maps of the r.m.s velocity field in figure 10 reveal interesting features. As the oscillation frequency increased, the measured r.m.s levels continued

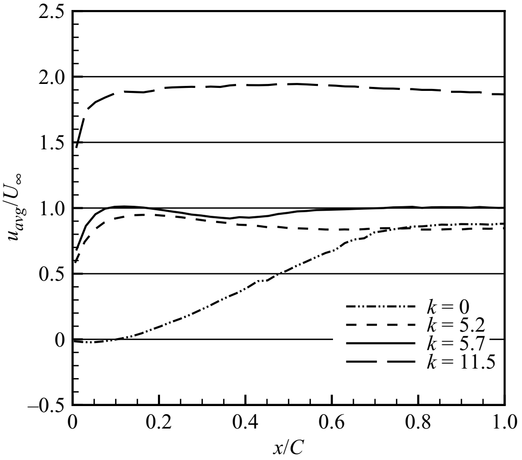

FIGURE 11. Downstream variation of the mean streamwise velocity at centreline ($y = 0$) for the cases shown in figure 10.

to increase and reached very large values, as high as $u_{r.m.s} \approx 0.75\ U_\infty$ for $k = 11.5$. The case of $k = 5.7$ was unique in that the streamwise velocity fluctuation approached zero at the centreline as expected for an alternating vortex array that is aligned along a straight line. The highest reduced frequency ($k = 11.5$) had a triple-peak structure with the weakest peak at the centreline. A similar structure also existed over a portion of the downstream range for the case of $k = 5.2$. It can be shown that the streamwise velocity fluctuation develops a third peak at the centreline depending on the transverse separation b of the vortex array in relation to the vortex core size.

We complete the discussion in this section by presenting the transverse profiles of the mean streamwise velocity $u_{avg}(y)$ and the r.m.s profiles of streamwise and transverse velocity fluctuations, $u_{r.m.s}(y)$ and $v_{r.m.s}(y)$, at a given downstream location (see figures 12, 13). Data at $x/C = 1$ were chosen for discussion as they relate to the calculation of the mean force in the next section (§ 3.3).

The mean streamwise velocity profiles depicted in figure 12 provide a quantitative assessment of the changes in the velocity profile as a result of the vortex array modification with increasing oscillation frequency. The static and low reduced frequency case ($k = 5.2$, for which $b < 0$) showed a mean velocity deficit or 'wake' profile, whereas the high reduced frequency case ($k = 11.5$ for which $b > 0$) showed a significant velocity excess or 'jet' profile. For the special case, $k = 5.7$, where the vortices were aligned nearly perfectly along a straight line (i.e. $b \approx 0$), the mean profile was uniform with speed U_∞. The mean transverse velocity profiles $v_{avg}(y)$, not included here, were nearly zero (see Bohl 2002). The data over the measurement domain $-0.3 < y/C < 0.3$ typically had an average value less than $0.006\ U_\infty$ and varied across the domain by less than $0.009\ U_\infty$.

The r.m.s profiles of streamwise and transverse velocity fluctuations, $u_{r.m.s}(y)$ and $v_{r.m.s}(y)$, at $x/C = 1$ are depicted in figure 13. The $u_{r.m.s}(y)$ profiles were characterized primarily by a double-peak structure whose peak level increased with increasing oscillation frequency. This was caused by the high streamwise velocity fluctuations on the top and bottom of the vortex array. For the highest frequency case a third small peak appeared at the centreline, a feature that was already discussed in the spatial maps in figure 10. When the vortex array was aligned nearly perfectly ($k = 5.7$),

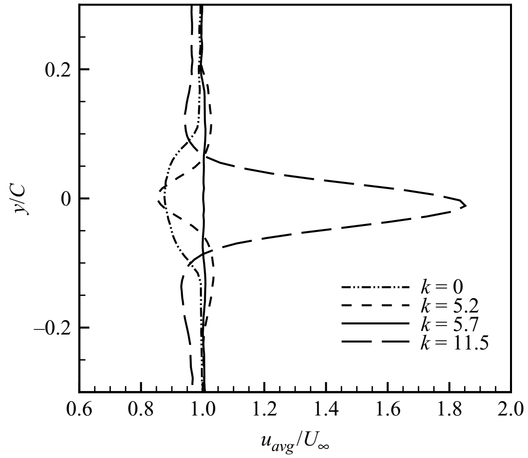

FIGURE 12. Mean streamwise velocity profiles at $x/C = 1$ for the static and oscillating airfoil for three reduced frequencies, $\alpha_o = 2°$.

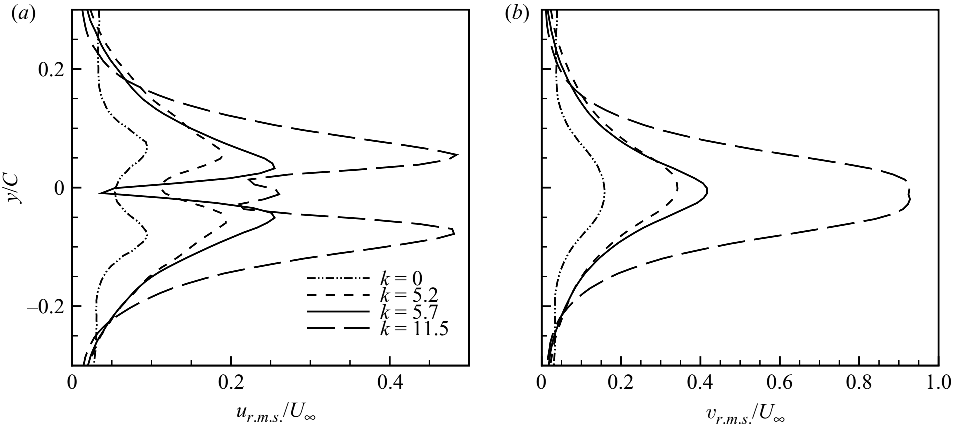

FIGURE 13. Profiles of r.m.s velocity fluctuations, (*a*) $u_{r.m.s}$ and (*b*) $v_{r.m.s}$, at $x/C = 1$ for the static and oscillating airfoil for three reduced frequencies, $\alpha_o = 2°$.

the streamwise velocity fluctuation at the centreline approached a very low level. A perfectly aligned alternating vortex array would have zero streamwise velocity fluctuation at centreline since the induced velocity would be in the transverse direction only. The transverse velocity fluctuation profiles $v_{r.m.s}(y)$ showed peak magnitudes that varied between 0.35 U_∞ and 0.9 U_∞ as the pitching frequency increased. We note that the fluctuations in the transverse velocity were significantly larger than the streamwise velocity by nearly a factor of 2.

3.3. *Mean force*

The mean streamwise force on the airfoil (i.e. drag/thrust) can be obtained from the integral momentum theorem applied to a control volume surrounding the airfoil. Traditionally, the mean streamwise velocity profile in the wake is utilized to estimate the force coefficient according to

$$C_F = \frac{2}{C}\int_{-H}^{+H} \frac{u_{avg}}{U_\infty}\left(\frac{u_{avg}}{U_\infty} - 1\right) \mathrm{d}y. \tag{7}$$

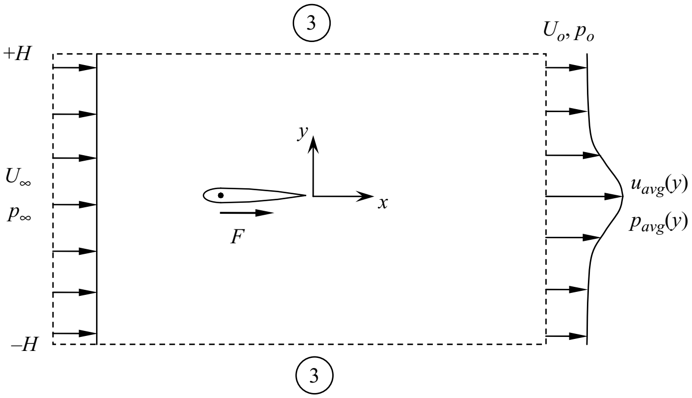

FIGURE 14. Control volume definition for analysis of mean thrust generated by pitching airfoil.

A negative value of C_F corresponds to drag and a positive value indicates thrust. In using this expression it is understood that the contributions from the velocity fluctuation and the pressure term are ignored and that the domain of integration H is selected sufficiently far away such that the integrand approaches zero. In the original work of Koochesfahani (1989), (7) was utilized since only the mean velocity profiles were available at that time. The subsequent computations of Ramamurti and Sandberg (2001) for the cases investigated by Koochesfahani (1989) reported thrust values that were significantly lower and the discrepancy was attributed to the missing terms in (7). In the work described here, a more complete analysis is carried out to compute the force coefficient from experimental data, which also allows us to assess the influence of the missing terms in (7).

Figure 14 shows a schematic of the control volume and the various parameters used in our two-dimensional analysis. The average pressure profile $p_{avg}(y)$ at the downstream control surface is needed for completing the mean force calculation. Considering the y-component of the mean Navier–Stokes equation, it can be shown that

$$\frac{\partial p_{avg}}{\partial y} = -\rho \frac{\partial v_{r.m.s}^2}{\partial y} \tag{8}$$

if the mean transverse velocity v_{avg} and streamwise gradient (i.e. $\partial/\partial x$) of Reynolds stress are negligible. Using the whole-field velocity data from our measurements, it was confirmed that at location $x/C = 1$, which we use for mean force calculation, these were, in fact, excellent assumptions. Our measurement domain corresponded to $H/C = 0.3$ and resulted in a ‘free stream’ speed U_o at the downstream location which was slightly different from the upstream speed U_∞. It was found that U_o/U_∞ varied between about 1.02 and 0.95 with increasing reduced frequency (e.g. see figure 12). The fact that the integration domain H was not far enough (i.e. $U_o \neq U_\infty$) led to two consequences. Firstly, the free stream pressure p_o at the downstream location was different from p_∞ by an amount that was determined from Bernoulli’s equation, i.e. $p_o = p_\infty + 1/2\ \rho(U_\infty^2 - U_o^2)$, resulting in the downstream average pressure distribution being given by

$$p_{avg}(y) = p_\infty + \tfrac{1}{2}\rho\left(U_\infty^2 - U_o^2\right) - \rho\, v_{r.m.s}^2(y). \tag{9}$$

Considering the large values of transverse velocity fluctuations especially at high reduced frequencies (see figure 13), the average pressure distribution downstream is expected to have a significant pressure deficit.

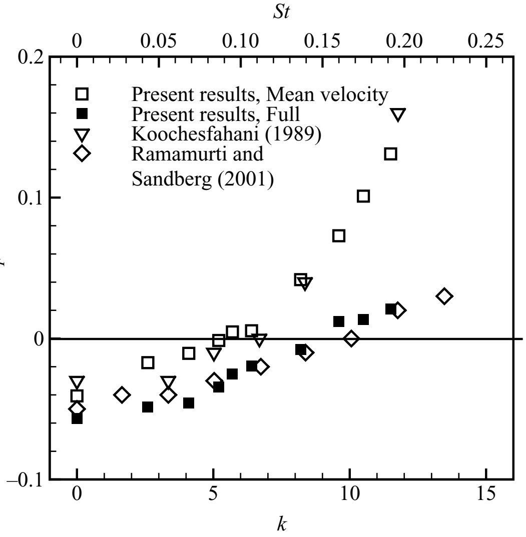

FIGURE 15. Airfoil mean force coefficient as a function of reduced frequency. Results are shown on the basis of only the mean velocity (term I in 10) and also the full (10). Comparison is made with the results of Koochesfahani (1989) based on mean velocity and computations of Ramamurti and Sandberg (2001).

The second consequence concerns the calculation of the x-component of momentum flux through control surfaces (3); see figure 14. In traditional analysis, with H being far away, the streamwise velocity u_3 on those surfaces would be U_∞. In the current analysis, however, u_3 varies between U_∞ upstream and U_o downstream. We estimate the x-component of momentum flux through control surfaces (3) using the mass flux, found the usual way from the balance of upstream and downstream mass fluxes, and an effective u_3 given by $u_3 = 1/2\ (U_\infty + U_o) \equiv (1-\varepsilon)U_\infty$. The value of ε varied between –0.01 and 0.025 over the range of reduced frequencies investigated here. The influence of the momentum flux approximation given here on the calculation of force coefficient was small because of the small deviation of U_o from U_∞. The largest uncertainty in C_F was found to be about ± 0.002 based on comparing the result using the $u_3$approximation given above versus those arrived at using the limiting values of U_∞ and U_o. This uncertainty occurred at the highest reduced frequency $k = 11.5$ (i.e. largest ε) and corresponded to about 10 % of the C_F value (see figure 15). The percentage uncertainly quickly dropped with decreasing frequency; for example, at $k = 5.7$ the uncertainty had reduced to about 1 %.

Incorporating the various influences described above, and the streamwise velocity fluctuation, into the control volume analysis around the airfoil results in the following expression for the force coefficient

$$\begin{aligned} C_F = \frac{2}{C}\int_{-H}^{+H} \Bigg\{ & \underbrace{\frac{u_{avg}}{U_\infty}\left(\frac{u_{avg}}{U_\infty}-1\right)+\varepsilon\left(\frac{u_{avg}}{U_\infty}-1\right)}_{\mathrm{I}} \\ & \underbrace{+\left(\frac{u_{r.m.s}}{U_\infty}\right)^2}_{\mathrm{II}}\underbrace{-\left(\frac{v_{r.m.s}}{U_\infty}\right)^2}_{\mathrm{III}}\underbrace{+\frac{1}{2}\left(1-\frac{U_o^2}{U_\infty^2}\right)}_{\mathrm{IV}}\Bigg\}\,\mathrm{d}y. \end{aligned} \qquad (10)$$

We note that term I represents the contribution from the mean streamwise velocity profile (i.e. 7) but modified to accommodate the slight variation of streamwise velocity along control surfaces (3) in figure 14. We also note that the fluctuation in the streamwise velocity serves to increase the thrust estimate, whereas the downstream pressure profile represented by the transverse velocity fluctuation reduces the estimated thrust.

Figure 15 summarizes the mean force coefficient calculated from the measured data as a function of reduced frequency. Results are shown based on using only the mean streamwise velocity, i.e. term I in (10) and also the full form of (10). Figure 16 shows the contribution of each term in (10) to the overall calculation of the force coefficient. Several aspects of these results are noteworthy. The mean force calculated based on only mean velocity data agrees very well with the previous estimates of Koochesfahani (1989) which were also arrived at in the same manner. The important conclusion is that the mean force, when calculated using the full (10), is in reality significantly lower and agrees remarkably well with the computations of Ramamurti and Sandberg (2001). The reduction of the mean force is particularly important at the higher reduced frequencies where the velocity fluctuations become very strong (see figure 13). On the basis of our measurements and a term-by-term analysis of (10), see figures 13 and 16, it is now clear that the increase in mean force due to the streamwise velocity fluctuation $u_{r.m.s}$ is strongly counteracted by the much larger transverse velocity fluctuation $v_{r.m.s}$ responsible for lowering the downstream pressure, resulting in a net reduction of mean force. We note that the reduced frequency for crossover from drag to thrust was calculated to be about $k \approx 6$ based on mean velocity data (i.e. using Term I only) and corresponded to the flow with an aligned alternating vortex array ($b = 0$). However, the actual reduced frequency for the crossover was found to be $k \approx 9$ using the full (10). At this reduced frequency the mean streamwise profile is already jet-like. This extra momentum flux is required to overcome the pressure reduction downstream of the oscillating airfoil. Comparison of our results with the computations of Ramamurti and Sandberg (2001) is limited only to the mean force data shown in figure 15 since Ramamurti and Sandberg (2001) did not report the details of the computed vorticity field. It is clear, however, that the spatial arrangement of the vortex array behind an oscillating object cannot by itself be used to determine the condition for drag-to-thrust crossover.

4. Conclusions

The structure of the flow and vorticity field around a NACA-0012 airfoil oscillating at small amplitude ($\alpha_o = 2^\circ$) and high reduced frequencies (up to $k = 11.5$) was investigated over the first chord length downstream of the airfoil trailing edge using MTV. The characteristics of the vortex array were quantified in terms of its spatial arrangement, the vortex core size, peak vorticity and circulation. The properties of the mean and fluctuating velocity and vorticity fields were quantified and explained on the basis of the unique spatial arrangement of the vortex array in each case.

The transverse alignment of the vortices was found to be a function of the reduced frequency with the orientation switching for $k > 5.7$. This switch in the vortex array orientation was marked by a change in the mean streamwise velocity from a velocity deficit (i.e. wake profile) to a velocity excess (jet-like profile). An important finding was that the switch in the vortex array orientation did not determine the condition for crossover from drag to thrust. The mean force on the airfoil was estimated from a more complete control volume analysis, which took into account the streamwise

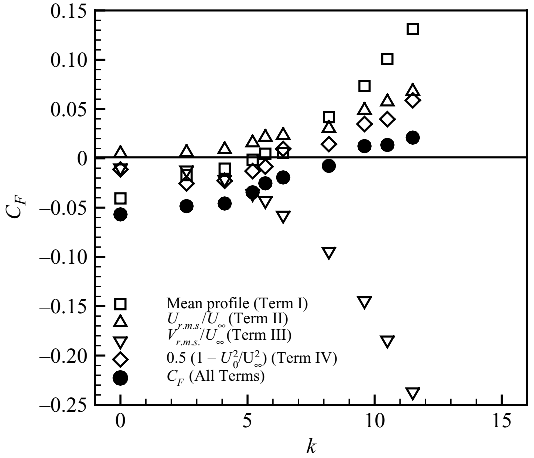

FIGURE 16. Contribution of individual terms in (10) to the overall force coefficient.

velocity fluctuations and the pressure term. Results clearly showed that it is critical to include these terms in the calculations, especially for strongly fluctuating velocity fields characteristic of airfoils executing highly unsteady motions. Otherwise, the mean force could be overestimated by a large margin.

The peak vorticity of the convecting vortices showed a decrease with downstream distance more than could be attributed to the effects of viscous diffusion. This behaviour could be explained using the vorticity transport equation and the presence of a small value of axial velocity gradient within the vortex cores. An interesting observation was that the three-dimensional effects caused by such small values of velocity gradient, which would be difficult to measure experimentally, could still lead to a measurable decrease in the peak vorticity even at the centre of the flow facility in a flow that was ‘expected’ to be primarily two-dimensional.

Several intriguing phenomena were noted that require further comments. For a particular value of reduced frequency, the alternating vortex array was almost perfectly aligned along a straight line. A consequence of this arrangement was that the mean streamwise velocity profile was uniform at the same speed as the upstream approach speed and the streamwise velocity fluctuations reduced to zero at the centreline. The implication of this result is that a velocity probe (designed to measure the streamwise velocity) which happens to be located at the centreline would not be able to detect the presence of a highly unsteady airfoil farther upstream. We note that the vortex array spacing *b* exhibited interesting dynamics during the initial formation process before approaching an asymptotic state. Depending on the reduced frequency, the spacing initially increased to various degrees, or showed a wavy pattern, before it finally approached a fixed spacing. Our experiments do not have sufficient spatial resolution very near the trailing edge to shed light on the underlying phenomena behind these observations. Further experimental and/or computational studies are needed to explain these observations based on the flux of vorticity originating at the airfoil trailing edge and the subsequent vorticity roll-up and dynamics.

This work was supported by the MRSEC program of the National Science Foundation, Award Numbers DMR-9400417 and DMR-9809688.

Appendix

Estimate of uncertainty in spanwise vorticity

Spanwise vorticity ω_z is calculated from the measured (u, v) velocity using a fourth order accurate central finite difference scheme, given by

$$(\omega_z)_{i,j} = \left(\frac{\partial v}{\partial x}\right)_{i,j} - \left(\frac{\partial u}{\partial y}\right)_{i,j},$$

where

$$\left(\frac{\partial v}{\partial x}\right)_{i,j} = \frac{-v_{i+2,j} + 8v_{i+1,j} - 8v_{i-1,j} + v_{i-2,j}}{12h}$$

and

$$\left(\frac{\partial u}{\partial y}\right) = \frac{-u_{i,j+2} + 8u_{i,j+1} - 8u_{i,j-1} + u_{i,j-2}}{12h}.$$

The data spacing, h, is a known constant; therefore, the calculated vorticity depends on eight variables: four transverse velocities (each with uncertainty δv) and four streamwise velocities (each with uncertainty δu). In the measurements discussed here, $\delta v \approx \delta u$. Standard uncertainty analysis allows the determination of the uncertainty in spanwise vorticity, $\delta\omega_z$, according to

$$(\delta\omega_z)^2 = \sum_{n=1}^{8} \left(\frac{\partial \omega_z}{\partial \chi_n}\delta\chi_n\right)^2, \qquad (1)$$

where χ_n and $\delta\chi_n$ represent the nth independent variable and its uncertainty, respectively. Carrying out the uncertainty analysis using the vorticity definition and the finite difference formulation of velocity derivatives given above leads to the final result

$$\delta\omega_z = \frac{1.34}{h}\delta u.$$

REFERENCES

Anderson, J. M., Streitlien, K., Barrett, D. S. & Triantafyllou, M. S. 1998 Oscillating foils of high propulsive efficiency. *J. Fluid. Mech.* **360**, 41.

Bohl, D. G. 2002 Experimental study of the 2-D and 3-D structure of a concentrated line vortex. PhD thesis, Department of Mechanical Engineering, Michigan State University, East Lansing, Michigan.

Bohl, D. G. & Koochesfahani, M. M. 2004 MTV measurements of axial flow in a concentrated vortex core. *Phys. Fluids.* **16** (9), 4185.

Cohn, R. K. 1999 Effects of forcing on the vorticity field in a confined wake. PhD thesis, Department of Mechanical Engineering, Michigan State University, East Lansing, Michigan.

Cohn, R. K. & Koochesfahani, M. M. 1993 Effect of boundary conditions on axial flow in a concentrated vortex core. *Phys. Fluids.* A **5** (1), 280.

Cohn, R. K. & Koochesfahani, M. M. 2000 The accuracy of remapping irregularly spaced velocity data onto a regular grid and the computation of vorticity. *Experiments Fluids* **29**, S61.

Dabiri, J. O., Colin, S. P., Costello, J. H. & Gharib, M. 2005 Flow patterns generated by oblate medusan jellyfish: field measurements and laboratory analyses. *J. Exp. Biol.* **208**, 1257.

DeLaurier, J. D. & Harris, J. M. 1982 Experimental study of oscillating-wing propulsion. *J. Airc.* **19** (5), 368.

Freymuth, P. 1988 Propulsive vortical signature of plunging and pitching airfoils. *AIAA J.* **26**, 881.

GENDRICH, C. P. 1998 Dynamic stall of rapidly pitching airfoils: MTV experiments and Navier–Stokes simulations. PhD thesis, Department of Mechanical Engineering, Michigan State University, East Lansing, Michigan.

GENDRICH, C. P., BOHL, D. G. & KOOCHESFAHANI, M. M. 1997 Whole-field measurements of unsteady separation in a vortex ring wall interaction. *AIAA Paper* 97-1780.

GENDRICH, C. P. & KOOCHESFAHANI, M. M. 1996 A spatial correlation technique for estimating velocity fields using molecular tagging velocimetry (MTV). *Experiments Fluids* **22**, 67.

GENDRICH, C. P., KOOCHESFAHANI, M. M. & NOCERA, D. G. 1997 Molecular tagging velocimetry and other novel applications of a new phosphorescent supramolecule. *Experiments Fluids* **23**, 361.

JONES, K. D. & PLATZER, M. F. 1997 Numerical computation of flapping wing propulsion and power extraction. *AIAA Paper* 97-0826.

KATZ, J. & WEIHS, D. 1978 Behavior of vortex wakes from oscillating airfoils. *J. Airc.* **15** (12), 861.

KOOCHESFAHANI, M. M. 1989 Vortical patterns in the wake of an oscillating airfoil. *AIAA J.* **27**, 1200.

KOOCHESFAHANI, M. M. (ed). 2000 Special feature: molecular tagging velocimetry. *Meas Sci Technol.* **11**, 1235.

KOOCHESFAHANI, M. M. & NOCERA, D. G. 2007 Molecular tagging velocimetry. In *Handbook of Experimental Fluid Dynamics* (ed. J. Foss, C. Tropea & A. Yarin), Chapter 5.4. Springer-Verlag.

LIGHTHILL, J. 1975 *Mathematical Biofluiddynamics*, SIAM.

LIU, H. & KAWACHI, K. 1999 A numerical study of undulatory swimming. *J. Comput. Phys.* **155**, 223.

McCroskey, W. J. 1982 Unsteady airfoils. *Annu. Rev. Fluid. Mech.* **14**, 285.

OSHIMA, Y. & OSHIMA, K. 1980 Vortical flow behind an oscillating foil. In *Proc. 15th IUTAM Intl Congress*, North Holland, 357.

PLATZER, M., NEACE, K. & PANG, C. K. 1993 Aerodynamic analysis of flapping wing propulsion. *AIAA Paper* 93-0484.

RAMAMURTI, R. & SANDBERG, W. 2001 Simulation of flow about flapping airfoils using finite element incompressible flow solver. *AIAA J.* **39**, 253.

ROSÉN, M., SPEDDING, G. R. & HEDENSTRÖM, A. 2004 The relationship between wingbeat kinematics and vortex wake of a thrush nightingale. *J. Exp. Biol.* **207**, 4255.

SPEDDING, G. R., HEDENSTRÖM, A. & ROSÉN, M. 2003 Quantitative studies of the wakes of freely flying birds in a low-turbulence wind tunnel. *Experiments Fluids* **34**, 291.

STANEK, M. J. & VISBAL, M. R. Study of the vortical wake pattern of an oscillating airfoil. *AIAA Paper* 89-0554.

STREITLIEN, K. & TRIANTAFYLLOU, G .S. 1998 On thrust estimates for flapping airfoils. *J. Fluids Struct.* **12**, 47.

THEODORSEN, T. 1935 General theory of aerodynamic instability and the mechanism of flutter. NACA TR 496. http://ntrs.larc.nasa.gov/search.jsp.

TRIANTAFYLLOU, G. S., TRIANTAFYLLOU, M. S. & GROSENBAUGH, M .A. 1993 Optimal thrust development in oscillating foils with application to fish propulsion. *J. Fluids Struct.* **7**, 205.

VON KÁRMÁN, T. & BURGERS, J. M. 1943 General aerodynamic theory—perfect fluids. In *Aerodynamic Theory* (ed. W. F. Durand), Division E, vol. II, p. 308. Springer-Verlag.

VON KÁRMÁN, T. & SEARS, W. R. 1938 Airfoil theory for non-uniform motion. *J. Aeronaut. Sci.* **5** (10), 379.

WILDER, M. C., MATHIOULAKIS, D. S., POLING, D. R. & TELIONIS, D. P. 1996 The formation and internal structure of coherent vortices in the wake of a pitching airfoil. *J. Fluids Struct.* **10**, 3.

WU, T. Y. 1971 Hydromechanics of swimming of fishes and cetaceans. *Adv. Appl. Mech.* **11**, 1.